Supplementary Materials for

CO₂ electrolysis to multicarbon products in strong acid

Jianan Erick Huang†, Fengwang Li†*, Adnan Ozden†, Armin Sedighian Rasouli,
F. Pelayo García de Arquer, Shijie Liu, Shuzhen Zhang, Mingchuan Luo,
Xue Wang, Yanwei Lum, Yi Xu, Koen Bertens, Rui Kai Miao, Cao-Thang Dinh,
David Sinton*, Edward H. Sargent*

†These authors contributed equally to this work.
*Corresponding author. Email: ted.sargent@utoronto.ca (E.H.S.);
sinton@mie.utoronto.ca (D.S.); fengwang.li@sydney.edu.au (F.L.)

This PDF file includes:

Materials and Methods
Figs. S1 to S19
Tables S1 to S6
References

Materials and Methods

Catalysts and chemicals preparation

All the chemicals used for electrolytes, catalyst synthesis, and electrode preparation, including phosphoric acid (85%), potassium chloride, potassium phosphate monobasic, potassium sulfate, potassium iodide, potassium hydroxide, sulfuric acid, perchloric acid, Aquivion (D79-25BS), Cu nanoparticles (25 nm), carbon nanoparticles and graphite, were purchased from Sigma Aldrich. Nafion 117 membrane and platinum mesh (grid aperture of 0.98×1.4 mm; purity 99.95%) were purchased from Fuel Cell Store. The polytetrafluoroethylene (PTFE) gas diffusion layer with 450 nm pore size was purchased from Beijing Zhongxingweiye Instrument Co., Ltd. Deionized water (18.2 MΩ) was used for the preparation of all electrodes. Cu and Ag were sputtered onto the PTFE substrate using pure Cu and Ag targets (>99.99%) in a vacuum environment ($10^{-5} \sim 10^{-6}$ Torr) in an Angstrom Nexdep sputtering system. The deposition rate was kept constant at 1 Å/sec. The thickness of the catalyst layer was kept constant for all the electrodes at 300 nm. Cation-augmenting layer (CAL) is a 2 µm-thick homogeneous blend of carbon NPs (50 nm, Vulcan XC-72R) and Aquivion. The CAL-modified Cu was prepared by spray coating the CAL solution dispersed in methanol onto a 300 nm-Cu sputtered hydrophobic PTFE substrates. High-surface-area Cu-NPs/PFSA electrodes were prepared by spray coating the following dispersion onto a PTFE substrate with 300 nm sputtered Cu in sequence: 6 µm-thick homogeneous blend of Cu nanoparticles and Aquivion, a 2 µm-thick homogeneous blend of C NPs and Aquivion, and a 2 µm-thick homogeneous blend of graphite flakes (325 mesh, < 44 µm, 99%, Sigma Aldrich) and Aquivion.

Flow cell assembly

The flow cell setup was composed of three chambers: anolyte chamber, catholyte chamber, and gas flow chamber. The size of the electrode exposed was 1 cm x 1 cm. The cathode GDE of interest was clamped between catholyte chamber and gas diffusion chamber, with the substrate side facing the gas chamber and catalyst side facing the catholyte chamber. A Pt foil was employed in the anolyte chamber. The catholyte and anolyte chambers were separated by a cation exchange membrane (CEM, Nafion 117®). The catholyte chamber contained an Ag/AgCl reference electrode (3 M KCl).

Catholyte and anolyte were applied through separate silicone tubes that each connected to a peristaltic pump, offering a constant flow rate of approximately 10 mL/min. Electrolytes going through the pumps first entered each chamber from the bottom and exited from the top and flows back to their bulk electrolyte which forms a close cycle. For the gas supply, a digital mass flow controller (SmartTrack 100, Sierra) was connected to CO_2/N_2 gas cylinder to control the flow rate in gas flow chamber. The CO_2 gas and N_2 gas cylinders were purchased from Linde Gas.

Full-cell measurements were performed in a slim flow cell setup composed of three chambers: anolyte chamber, catholyte chamber, and gas flow chamber. As schematically illustrated in Figure S15, all chambers were designed to ensure a proximity between the cathode electrode and anode electrode to minimize the ohmic losses. We assembled the cell by separating the anode and cathode compartments using a CEM and applying an equal compression torque to each of four bolts. When assembled, the distances between the CEM and cathode electrode and the CEM and anode

electrode are both 1.5-2 mm. In the full cell system, we paired CO_2R cathode with an oxygen evolution reaction (OER) anode. We used the high-surface-area CAL-modified Cu electrodes for the CO_2R, and iridium oxide supported titanium (IrOx-Ti) felt electrodes for the OER. The IrOx loading was 1.5 mg/cm^2, akin to the typical loadings used in neutral media zero-gap electrolyzers (*40*).

Electrochemical measurement

All the electrochemical tests were carried out using an electrochemical workstation (Autolab PGSTAT302N) connected to a current booster (Metrohm Autolab, 10 A), except for the linear sweeping voltammetry (LSV) tests, which were performed via a CHI 660E potentiostat. The catholyte of pH 1 or lower was prepared using 1 M phosphoric acid as the base electrolyte, with the incorporation of different salts at various concentrations. The most frequently used salt was potassium chloride, with the highest concentration of 3 M.

The CO_2R performance was tested in a flow cell assembly under galvanostatic mode. 1 M phosphate buffer solutions with different salts and concentrations were used as the catholyte, and 1 M phosphoric acid was used as the anolyte. Cu on PTFE (300 nm), CAL-modified Cu and Cu-NPs/PFSA were used as the cathodes in different tests.

LSV was taken in the same flow cell setup that is used for performance evaluation, and the electrolytes were saturated with N_2 through continuous bubbling. Cu sputtered on PTFE (300 nm), Ag/AgCl (3 M KCl), and a Pt foil were used as the working electrode, reference electrode, and counter electrode, respectively. The scan rate was kept constant at 50 mV/s. Phosphate was used as the catholyte, in which the total phosphate concentration was kept constant at 1 M. 0.5 M H_2SO_4 was used as the anolyte. The cathode and anode chambers were separated by a CEM (Nafion® 117). For LSVs of different pH, the total potassium concentration was kept at 2 M to sustain a high ion conductivity and achieve high current density. In detail, the catholyte of pH 1 was prepared using 1 M H_3PO_4 and 2 M KCl, and the pH was adjusted to around 1 (0.96) by a few drops of 5 M KOH. The catholyte of pH 2 was prepared using 0.5 M H_3PO_4, 0.5 M KH_2PO_4, and 1.5 M KCl, and the pH was adjusted to 1.94 through the addition of KOH. The catholyte of pH 3 was prepared using 0.1 M H_3PO_4, 0.9 M KH_2PO_4, and 1.1 M KCl, and the pH was adjusted to 2.94 through the addition of KOH. The catholyte of pH 4 was prepared using 1 M KH_2PO_4, and 1 M KCl, and the pH was adjusted to 3.96 by KOH. For the LSVs of different concentrations of potassium, KCl was added to 1 M H_3PO_4 electrolyte to supply the desired concentration of potassium. The pH of 0, 1, 2, and 3 M potassium were 1.05, 0.85, 0.81, and 0.67, respectively. All potentials were converted to RHE scale via the equation:

$$E \text{ (RHE)} = E \text{ (Ag/AgCl)} + 0.059 \times \text{pH} + 0.210 + iR$$

where R is the resistance measured at open circuit potential and 80% of iR was compensated by the CHI software. Unless otherwise stated, the volumes of catholyte and anolyte used for circulation were 25 mL, and the liquid products were collected after 1 hour of continuous operation for analysis. The current densities reported are based on the geometric surface area.

Voltage loss breakdown study is experimentally measured for each factor (thermodynamic, pH gradient, ohmic resistance, cathodic and anodic overpotentials) using the three-electrode (Ag/AgCl, 3M KCl reference) flow cell setup at a constant current density of 1.2 A/cm^2 in acidic electrolyte

(1 M H_3PO_4 + 3 M KCl). The cathodic and anodic applied potentials (and thereby overpotentials) were measured using an Ag/AgCl reference electrode and were converted to RHE scale using the following equation:

$$E \text{ (vs. RHE)} = E \text{ (Ag/AgCl)} + 0.210 + 0.059 \times pH_{surface} + iR$$

where R of the anode and cathode, respectively, was measured by electrochemical impedance spectroscopy (EIS). It is noted that surface pH was used to exclude contributions from pH gradients. Nernstian loss due to pH gradient was quantified by comparing bulk pH and surface pH obtained from Comsol modelling via:

$$V_{Nernst} = 0.059 \times (pH_{surface} - pH_{bulk})$$

The overall ohmic resistance (including electrolytes and membrane) of the cell was measured by EIS.

Carbonate/CO₂ crossover test

CO_2 crossover was measured at a constant current density of 400 mA/cm² for 6 hours. For the neutral electrolyte, both anolyte and catholyte (25 mL for each) were 1 M $KHCO_3$, which were saturated with CO_2 prior to the experiment. For the acidic conditions, the anolyte (25 mL) was 0.5 M H_2SO_4, and the catholyte (25 mL) was 1 M phosphate buffer solution. 2 M of KCl was added to the catholyte to improve the ion conductivity. The CO_2 flow rate was kept constant at 50 sccm using a mass flow controller (Alicat Scientific). The gas products collected from the anodic outlet were analyzed by a gas chromatography (PerkinElmer Clarus 680). The pH of catholyte and anolyte were monitored by a pH meter.

CO₂RR product analysis

The gas products were collected from the gas outlet channel of the flow cell and injected into a gas chromatograph (PerkinElmer Clarus 680). The gas chromatograph was equipped with a thermal conductivity detector (TCD) for detection of H_2, O_2, N_2 and CO signals and a flame ionization detector (FID) for the detection of CH_4 and C_2H_4 signals. The gas chromatograph was composed of packed columns of Molecular Sieve 5A and Carboxen-1000 and employed Argon (Linde, 99.999%) as the carrier gas. For quantification, 1 mL of gas product was injected into the gas chromatograph, and the performance was evaluated as a function of current density, gas flow rate and gas products fraction.

$$\text{Faradaic efficiency (\%)} = N \times F \times v \times r / (i \times V_m)$$

where N is the number of electrons transferred, F is the Faradaic constant, v is the gas flow rate, r is the concentration of detected gas product in ppm, i is the total current, and V_m is the unit molar volume of gas. The gas flow rate was measured at the outlet of the gas chamber by a bubble flow meter.

The liquid products were analyzed using ^1H NMR spectroscopy (600 MHz Agilent DD2 NMR Spectrometer) with water suppression. We used dimethyl sulfoxide (DMSO) as the reference

standard and deuterium oxide (D_2O) as the lock solvent. The Faradaic efficiency was calculated using the equation below:

$$\text{Faradaic efficiency } (\%) = N \times F \times n_{product}/Q$$

where N is the number of electrons transferred, F is the Faradaic constant, $n_{product}$ is the total moles of products, and $Q = i \times t$ is the total charged passed during the experiment.

The single pass carbon efficiency (SPCE) of CO_2 towards each product or a group of products was determined using this equation at 25 °C, 1 atm:

$$\text{SPC} = (j \times 60 \text{ sec})/(N \times F) \div (\text{flow rate (L/min)} \times 1 \text{ (min)})/(24.05 \text{ (L/mol)})$$

where j is the partial current density of specific group of products from CO_2 reduction, N is the electron transfer for every product molecule.

Materials characterizations

Scanning electron microscopy (SEM) imaging was performed in a high-resolution scanning electron microscope (HR-SEM, Hitachi S-5200). X-ray photoelectron spectroscopy (XPS) measurements were carried out in an ECSA device (PHI 5700) with Al Kα X-ray energy source (1486.6 eV) for excitation. Prior to measurements, the catalysts were rinsed sequentially with 1 M H_3PO_4 and DI water to remove any potential residual salt from the surface. Operando hard X-ray absorption spectroscopy measurements were conducted at 9BM beamline of the Advanced Photon Source (APS, Argonne National Laboratory, Lemont, Illinois). The data were processed by Athena and Artemis software incorporated into standard IFEFFIT package.

Techno-economic analysis (TEA)

To assess the energy penalty and associated cost induced by CO_2 crossover, we considered two benchmark systems from literature: neutral and alkaline CO_2R electrolyzers. These neutral CO_2R MEA and alkaline flow cell electrolyzers were considered specifically owing to their performance metrics – industrially relevant reaction rates (>100 mA/cm^2), high FE towards C_{2+} products (i.e. an ethylene FE of >60%), and high full-cell energy efficiency (EE) towards C_{2+} products (i.e. an ethylene full-cell EE of >20%). We postulated that the proximity of these performance metrics for each system being compared (alkaline, neutral electrolyzers) will help refine the effect of CO_2 crossover and carbonate formation on the total energy requirement of producing C_{2+} products (i.e. ethylene). Table S1 summarizes the input parameters to the model for both systems, along with considerations of industrial costs. Majority of these input parameters were obtained from literature. The CO_2R performance of both MEA electrolyzers and alkaline flow cell electrolyzers are still improving, thus we considered optimistic performance metrics (current density, selectivity, and energy efficiency) towards a single C_2 product for each system. The techno-economic model considers a production rate of 1 ton per day, with assumptions that H_2 and O_2 are the only by-products coming out of the cathodic and anodic streams, respectively. Detailed calculations of cost, along with the main assumptions made, for the capital, installation, operation, carbon regeneration (for alkaline flow cell), cathode separation (for both the alkaline flow cell and MEA electrolyzers),

anode separation (for neutral MEA), can be found in our recent work (*38*). Table S2 presents the cost breakdown of alkaline flow cell electrolyzers and neutral MEA CO_2R electrolyzers.

Table S1. The operational cost breakdown of neutral CO_2RR MEA electrolyzer and alkaline flow-cell electrolyzer in ideal scenario.

Model input parameters	Neutral CO_2R in MEA	Alkaline CO_2R in flow cell
CO_2 input (\$/ton)	30	30
H_2O (\$/ton)	5	5
Electrolyte	0.1 M $KHCO_3$	3 M KOH
Electrolyte salts cost (\$/ton)	750	1000
Electrolyte lifetime (year)	1	1
Catalysts/Membrane lifetime (year)	5	5
System lifetime (year)	30	30
Electrolyzer cost (\$/kW)	300	300
Electricity cost (\$/kWh)	0.03	0.03
Balance of Plant (%)	50	50
Lang factor	1	1
Capacity factor	0.9	0.9
Cell voltage (V)	3.7	2.5
Faradaic efficiency (%)	95	95
Current density (A/cm^2)	0.2	0.2
Single pass conversion (%)	23.75	4.5
CO_2 crossover factor	3	20
Output product	C_2H_4	C_2H_4

Table S2. Techno-economic assessment of neutral CO_2R MEA electrolyzer and alkaline flow-cell electrolyzer, together with specific cost distribution per ton of ethylene produced.

Cost distribution	Alkaline flow cell (\$/ton)	Neutral MEA cell (\$/ton)
Electrolyzer capital	396.47	586.78
Electrolyzer installation	1125	1590.87
Electrolyzer Operation	264.32	391.19
Cathode separation	133.15	133.15
Carbonate regeneration	2317.54	0
Anode separation	0	509.79
Summation	4236.48	3211.78

COMSOL simulations

A reaction-diffusion model was used to simulate the local pH using COMSOL Multiphysics software. All the interactions between species in the electrolyte (CO_2, HCO_3^-, CO_3^{2-}, H_3PO_4,

$H_2PO_4^-$, HPO_4^{2-}, PO_4^{3-}, OH^-, H^+ and H_2O) were considered. We used Henry's law to calculate the CO_2 concentration[1], assuming that the CO_2 fugacity is 1 bar.

$$C^0_{CO2,aq} = K^0_H C^0_{CO2,gas}$$

K^0_H is the Henry's constant, which can be calculated by using the equation below, where T is the temperature (39).

$$\ln(K^0_H) = 93.4517 \times \frac{100}{T} - 60.2409 + 23.3585 \times \ln\left(\frac{T}{100}\right)$$

Due to the high concentration of the ions, the saturated concentration of CO_2 in an electrolyte is corrected using the following equations (39).

$$\log\left(\frac{C^0_{CO2,aq}}{C_{CO2,aq}}\right) = K_s C_s$$

where $K_s = \sum(h_{ion} + h_G)$

$$h_G = h_{G,0} + h_T(T - 298.15)$$

C_s is the molar concentration and K_s is the Sechenov's constant which can be estimated using equation S4-S5 and Table S3.

Table S3. Sechenov's Constant values. (39)

Constant	Value
$h_{G,0}$	-0.0172
h_T	-0.000338
h_K	0.0922
h_{Cl}	0.0318
h_{OH}	0.0839
h_{HCO3}	0.0967
h_{CO3}	0.1423
h_{H2PO4}	0.0906
h_{HPO4}	0.1499
h_{PO4}	0.2119

We considered the following homogeneous and heterogenous reactions in our model, which are based on the previously published works (40-44). The heterogenous reactions (reaction 1-4) take place in the porous catalyst layer, and the homogenous reactions (reaction 5-12) occur in entire domain (45).

$$2H_2O + 2e^- \rightarrow H_2 + 2OH^-$$

$$CO_2 + H_2O + 2e^- \rightarrow CO + 2OH^-$$

$$CO_2 + H_2O + 2e^- \rightarrow HCOOH + 2OH^-$$

$$CO_2 + H_2O + 8e^- \rightarrow CH_4 + 8OH^-$$

$$2CO_2 + 8H_2O + 12e^- \rightarrow C_2H_4 + 12OH^-$$

$$2CO_2 + 9H_2O + 12e^- \rightarrow C_2H_5OH + 12OH^-$$

$$CO_2 + H_2O \rightleftharpoons H^+ + HCO_3^-$$

$$HCO_3^- \rightleftharpoons H^+ + CO_3^{2-}$$

$$CO_2 + OH^- \rightleftharpoons HCO_3^-$$

$$HCO_3^- + OH^- \rightleftharpoons CO_3^{2-} + H_2O$$

$$H_2O \rightleftharpoons H^+ + OH^-$$
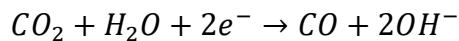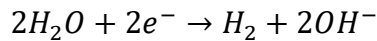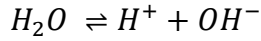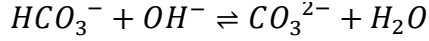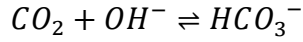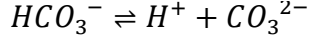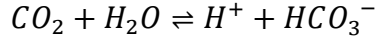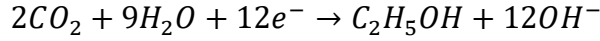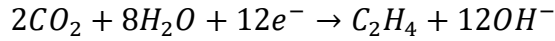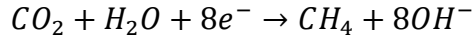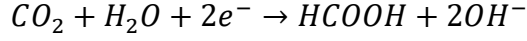
The bulk concentrations and pH values were measured experimentally and implemented in the model. The thickness of the diffusion layer was assumed to be 50 μm. The ion species transport is based on the reaction previously listed and follows the equation below. J_i is the molar flux. The species diffusion coefficients are listed in Table S4.

$$\frac{\partial c_i}{\partial t} + \frac{\partial J_i}{\partial x} = R_i$$

$$J_i = -\frac{D_i \partial c_i}{\partial x}$$

The heterogenous reactions were simulated by adding the electrochemical reaction rates to the equation as follow:

$$\frac{\partial c_i}{\partial t} + \frac{\partial J_i}{\partial x} + r_i = R_i$$

$$r_i = \begin{cases} r_{CO_2} = -\dfrac{i}{F}\left(\dfrac{FE_{CO}}{2} + \dfrac{FE_{HCOOH}}{2} + \dfrac{FE_{CH4}}{8} + \dfrac{FE_{C2H4}}{12} + \dfrac{FE_{C2H5OH}}{12}\right) \times \dfrac{\varepsilon}{L_{catalyst}} \\[4mm] r_{OH^-} = \dfrac{i}{F} \times \dfrac{\varepsilon}{L_{catalyst}} \end{cases}$$

An average product distribution was assumed, where S is approximated to 40% and X+Y+Z to 60% (Table S5). A porosity of 60%, ε, and length of the catalyst of 300 nm, $L_{catalyst}$, layer was considered in the model.

Using this approach, we have simulated from 20 mA/cm² to 1000 mA/cm² with intervals of 10 ~ 200 mA/cm² (10 ~ 25 mA/cm² for Figure 2A, and 50 ~ 200 mA/cm² for Figure S2).

Table S4. Diffusion coefficient values (*39, 46*).

Diffusion coefficient	Value (10^{-9} m²/s)
CO_2	1.91
CO_3^{2-}	0.923
HCO_3^-	1.185
H^+	9.31
OH^-	5.273
H_3PO_4	0.918
$H_2PO_4^-$	0.918
HPO_4^{2-}	0.458
PO_4^{3-}	0.612

Table S5. The assumed product distribution in the modeling.

Product	H_2	$CO + HCOOH$	CH_4	$C_2H_4 + C_2H_5OH$	Total FE
FE (%)	S	X	Y	Z	X+Y+Z+S
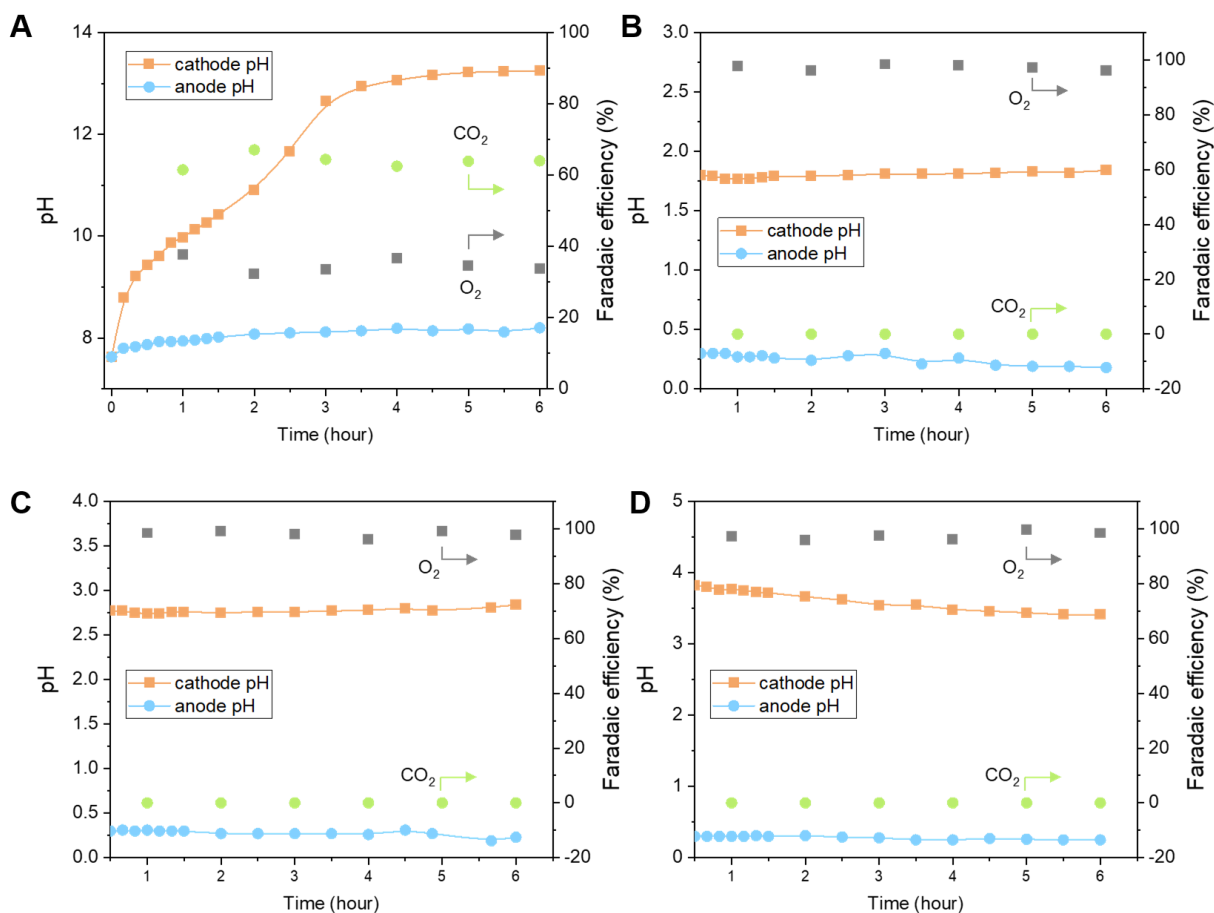
Fig. S1. CO$_2$ crossover tests in different electrolytes at a constant current density of 400 mA/cm^2. **(A)** 1 M KHCO$_3$ with AEM. Large amount of CO$_2$ crossover was observed in neutral media flow cell using 1 M KHCO$_3$. The gas exiting from the anode outlet has a composition of CO$_2$:O$_2$ around 7:3. **(B)** 0.5 M H$_3$PO$_4$ + 0.5 M KH$_2$PO$_4$ catholyte and 0.5 M H$_2$SO$_4$ anolyte with CEM. **(C)** 0.1 M H$_3$PO$_4$ + 0.9 M KH$_2$PO$_4$ and 0.5 M H$_2$SO$_4$ anolyte with CEM. **(D)** 1 M KH$_2$PO$_4$ and 0.5 M H$_2$SO$_4$ anolyte with CEM.
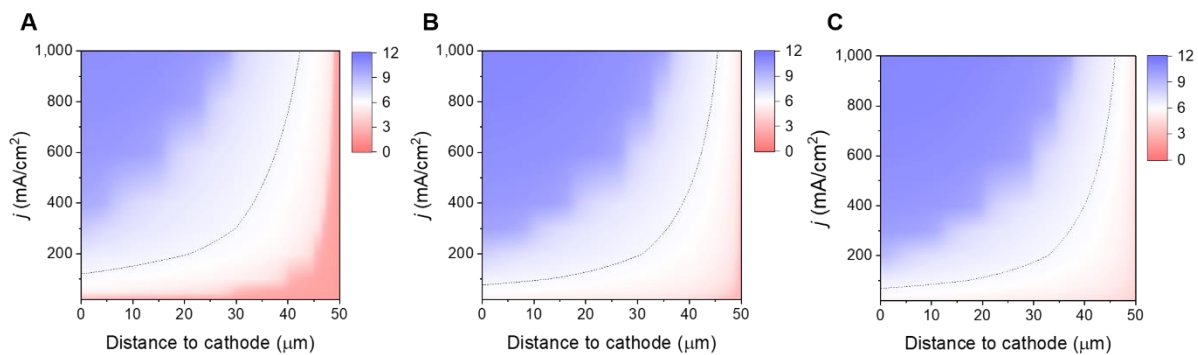
Fig. S2. Modelling of pH near the cathode for 1 M phosphate electrolyte of different bulk pH. (**A**) pH 1.94. (**B**) pH 3.02. (**C**) pH 3.96.
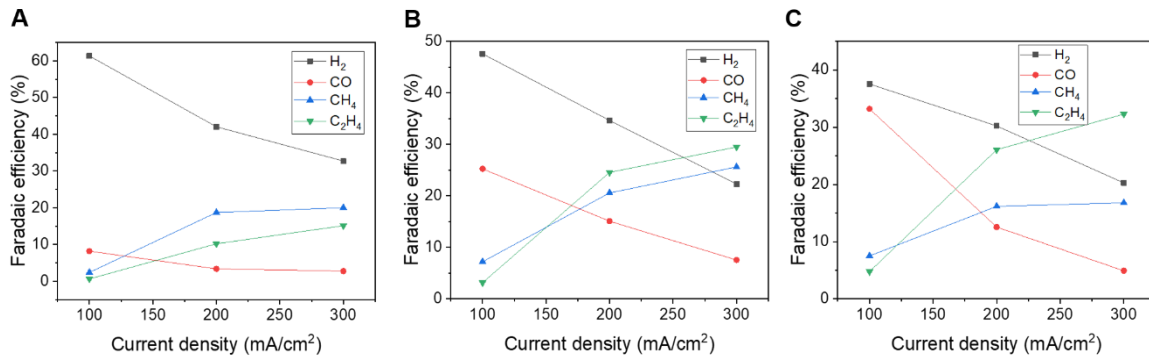
Fig. S3. Faradaic efficiency on sputtered Cu from 100 mA/cm^2 to 300 mA/cm^2 in 1 M phosphate electrolyte of different bulk pH. (A) pH 2. **(B)** pH 3. **(C)** pH 4.
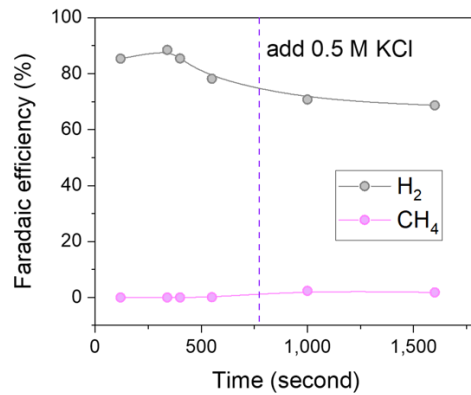
Fig. S4. Effect of KCl addition on the Faradaic efficiency of CH$_4$ and H$_2$ at 200 mA/cm^2.
When 0.5 M KCl was added into 1 M H$_3$PO$_4$, we observed a decrease in HER activity and a slight increase in CO$_2$RR activity towards CH$_4$.
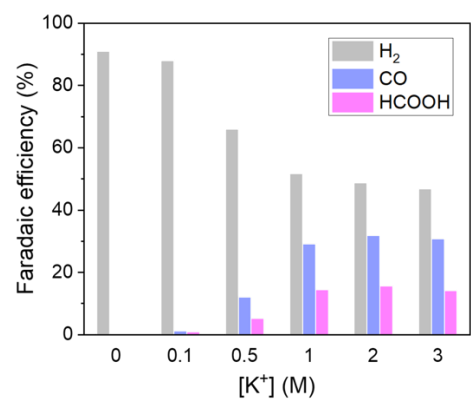
Fig. S5. Faradaic efficiency on sputtered Ag with different KCl concentrations at 400 mA/cm².
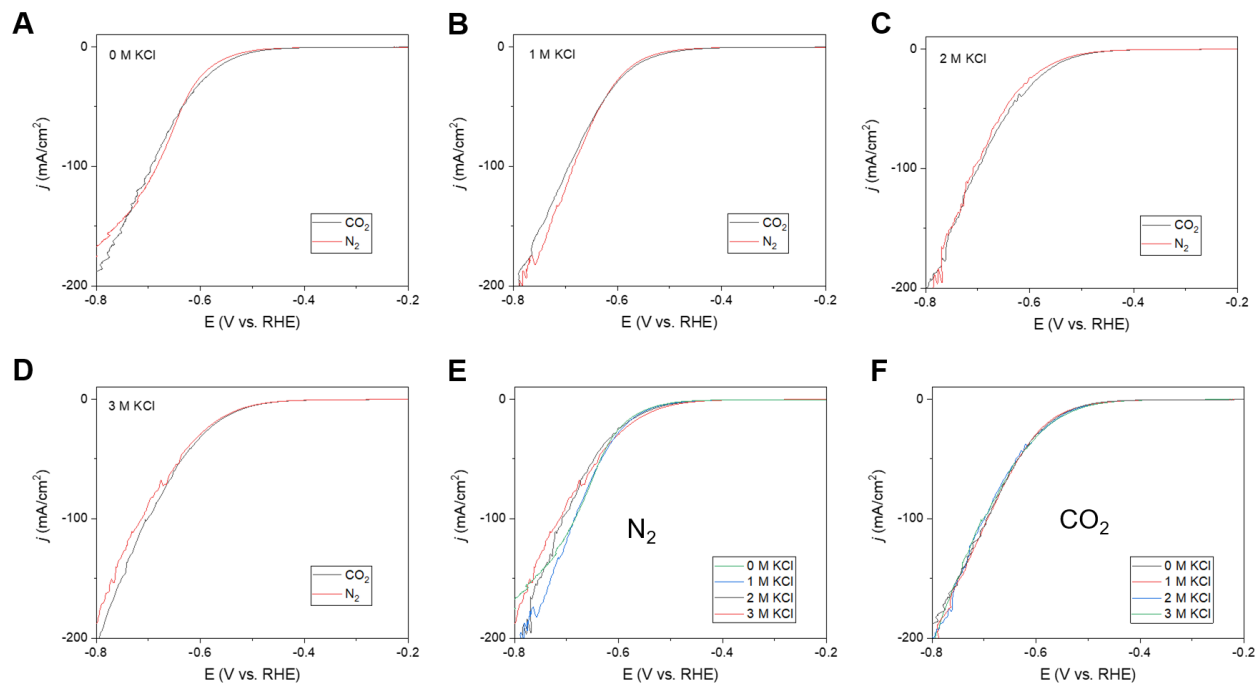
Fig. S6. The effect of K⁺ addition on voltametric responses of CO₂R and HER in 1 M H₃PO₄ electrolyte at current densities <200 mA/cm². (**A**) 1 M H_3PO_4. (**B**) 1 M H_3PO_4 + 1 M KCl. (**C**) 1 M H_3PO_4 + 2 M KCl. (**D**) 1 M H_3PO_4 + 3 M KCl. (**E**) Comparison of voltametric curves under N_2 flow. (**F**) Comparison of voltametric curves under CO_2 flow.
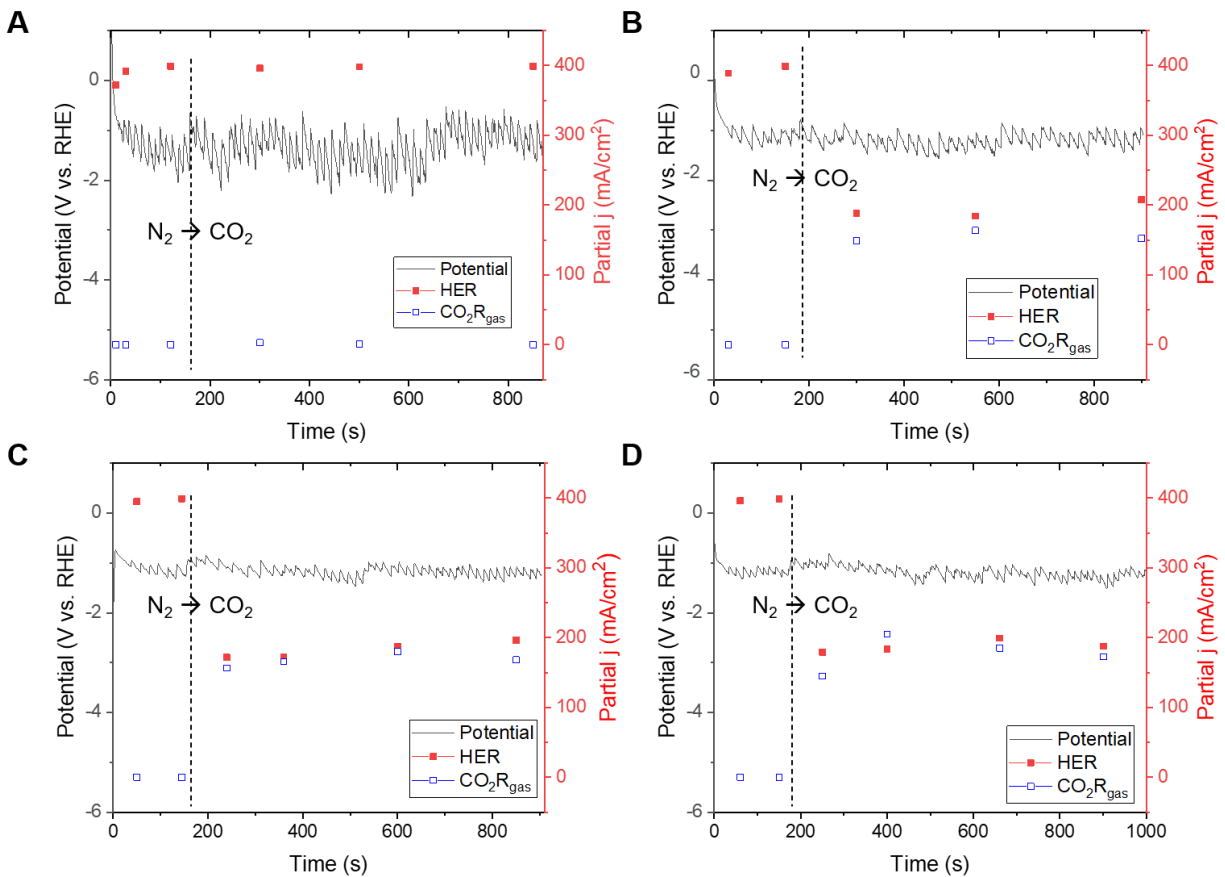
Fig. S7. The effect of K⁺ on CO₂R and hydrogen evolution current densities (total 400 mA/cm²). **The dashed line indicates the time of switching the gas flow from N₂ to CO₂. (A)** 1 M H_3PO_4. **(B)** 1 M H_3PO_4 + 1 M KCl. **(C)** 1 M H_3PO_4 + 2 M KCl. **(D)** 1 M H_3PO_4 + 3 M KCl.
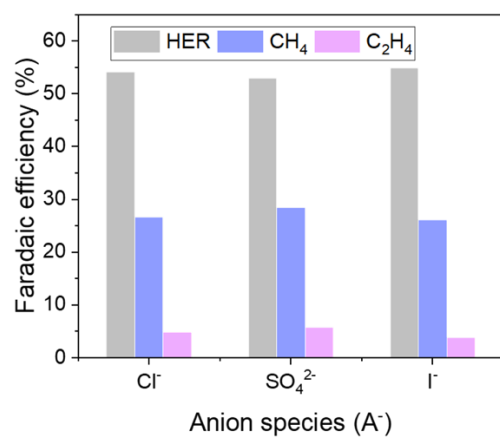
Fig. S8. Faradaic efficiency on the sputtered Cu under 400 mA/cm^2 in electrolytes of similar pH with different anions species. The electrolyte was 1 M H_3PO_4 solutions containing 1 M KCl, K_2SO_4 or KI.
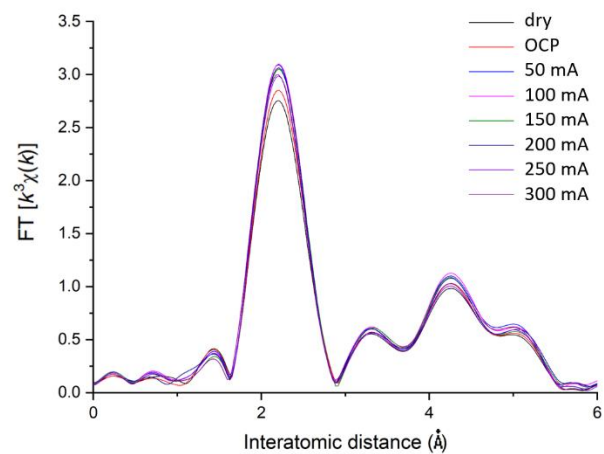
Fig. S9. In-situ XAS measurement on the sputtered Cu catalyst. The XAS spectra showed only coordination of metallic Cu. OCP (open circuit potential). The geometric area of the working electrode is 1 cm^2.
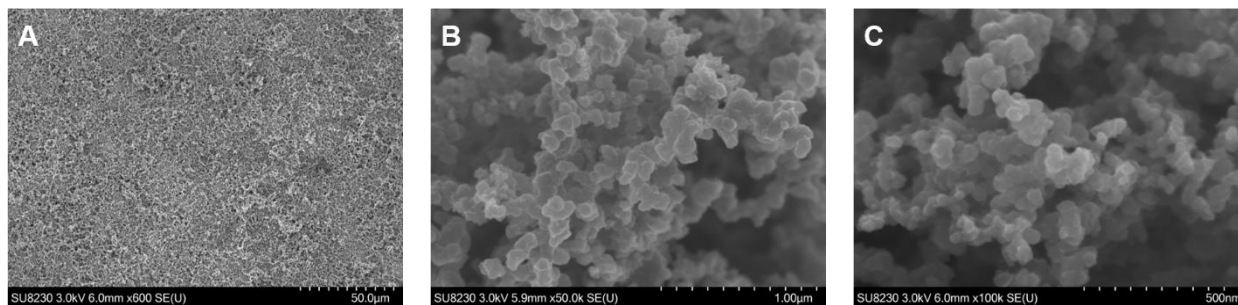
Fig. S10. SEM images of the high-surface area CAL-modified Cu-NPs/PFSA electrodes. (A-C) The Cu-NPs/PFSA electrodes are composed of C NPs blended with PFSA ionomers.
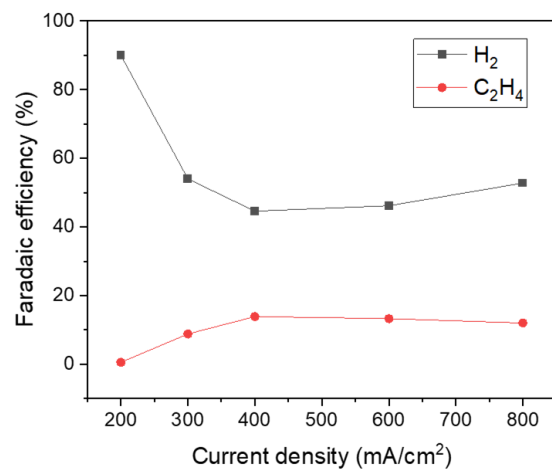
**Fig. S11. Faradaic efficiency towards C₂H₄ on CAL-modified Cu electrode from 200 mA/cm²
to 800 mA/cm² in 1 M H₃PO₄ + 3 M KCl electrolyte.** The C_2H_4 FE remains above 10% in a
current density range between 300 mA/cm² and 800 mA/cm².
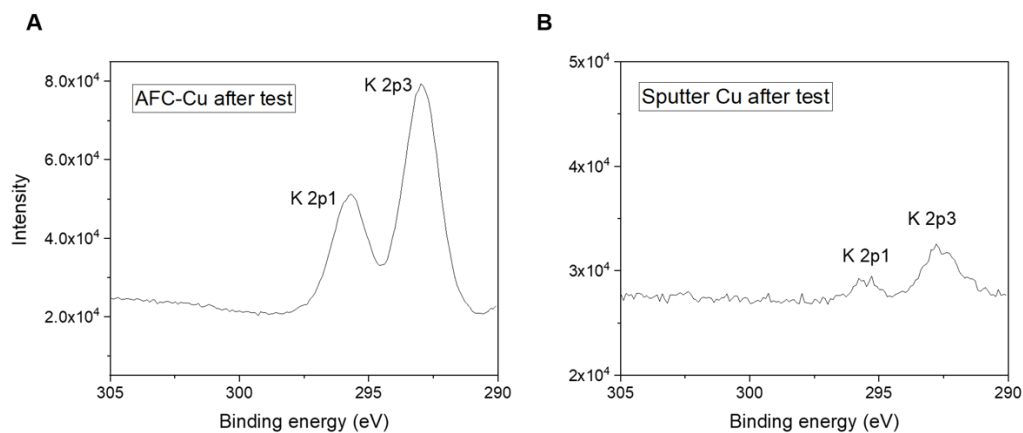
Fig. S12. K2p XPS of electrodes after testing in 1 M H₃PO₄ + 3 M KCl for 20 minutes. (A) CAL-modified Cu electrode. **(B)** Bare sputtered Cu electrode. A slight K content is detected on the surface of pure sputtered Cu upon completion of the test, which might be due to the crystalized salts from the electrolyte, while a large amount of K content was detected on the surface of the CAL-modified Cu electrode.
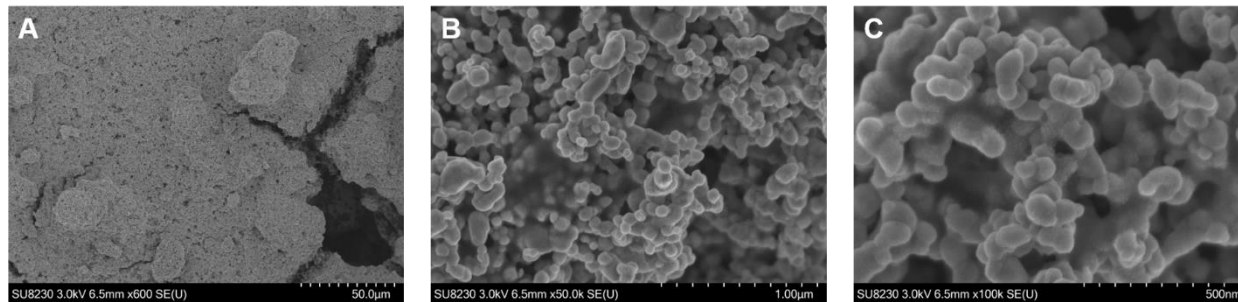
Fig. S13. SEM images of the high-surface-area CAL-modified Cu electrode. Cu NPs are surrounded by PFSA films.
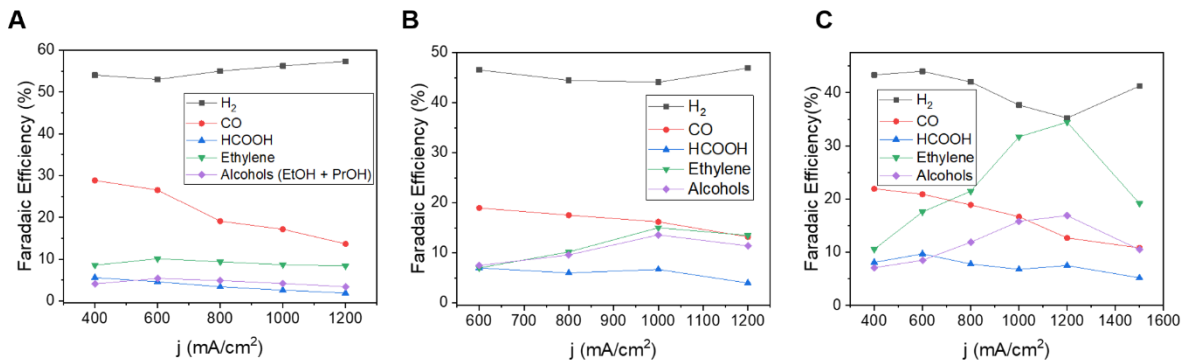
Fig. S14. Faradaic efficiency distributions on high-surface-area CAL-modified Cu electrodes at various current densities in 1 M H₃PO₄ electrolyte with different KCl concentrations. (A) 1 M KCl. **(B)** 2 M KCl. **(C)** 3 M KCl.
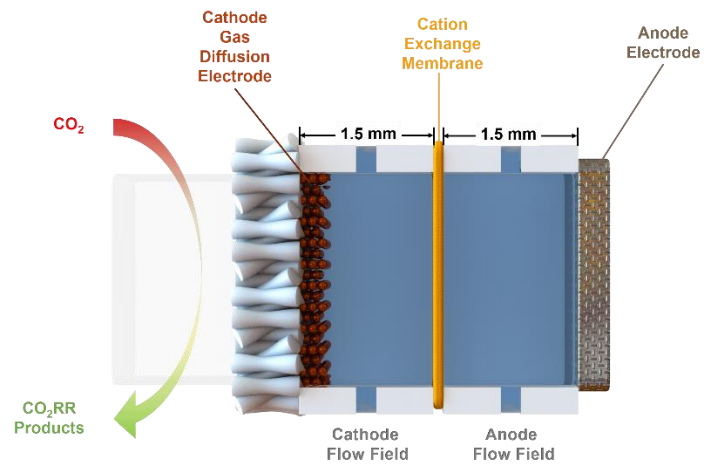
Fig. S15. Schematics of slim flow cell. The distance between cathode and anode electrodes is deliberately kept small (approximately 3 mm) to minimize solution resistance.
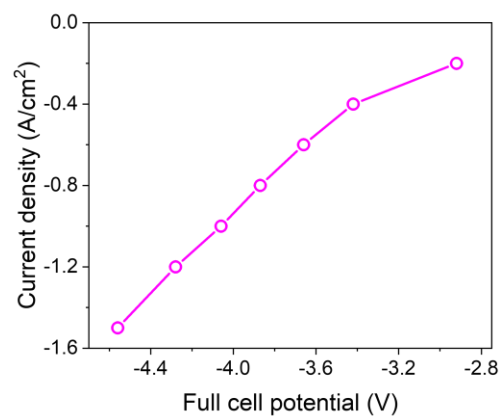
Fig. S16. *j*–V curve of high-surface-area CAL-modified Cu electrode in a slim flow cell. IrOx/Ti was used as the anode, and Nafion was used as the membrane. The full-cell voltages are presented without *i*R compensation.
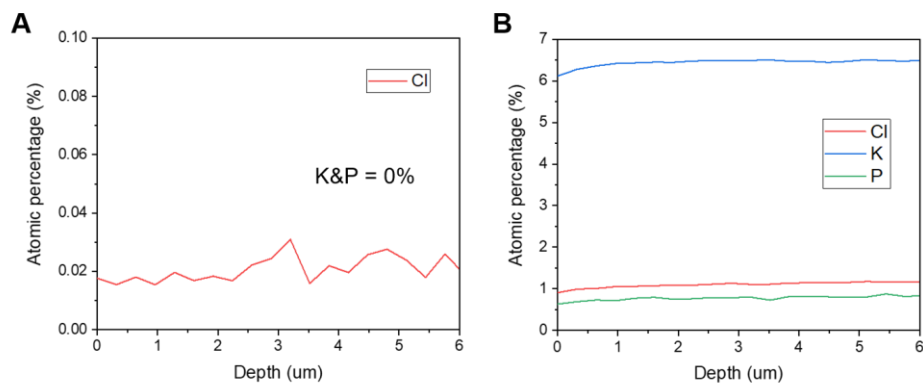
Fig. S17. In-depth elemental profile of high-surface-area CAL-modified Cu electrodes via sputtering XPS. (A) As made CAL-modified electrode. **(B)** CAL-modified electrode after CO_2R in 1 M H_3PO_4 and 3 M KCl electrolyte for 20 minutes at 1200 mA/cm^2. We observed an even distribution of K species within the catalyst layer after CO_2R, much higher content than the bias species Cl and P that come from the crystalized salts from the electrolyte. To prevent a bias that might come from crystalized KCl or potassium phosphate, we rinsed the surface with 0.1 M H_3PO_4 after the reaction.
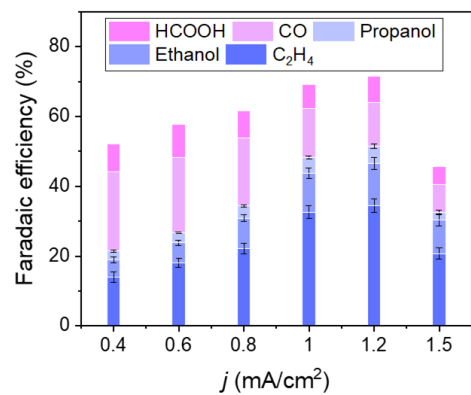
Fig. S18. Faradaic efficiency distributions toward CO₂R products from 400 to 1,500 mA cm⁻² on CAL-modified Cu-NPs/PFSA electrodes. The flow rate of CO₂ at the inlet was 5 sccm.
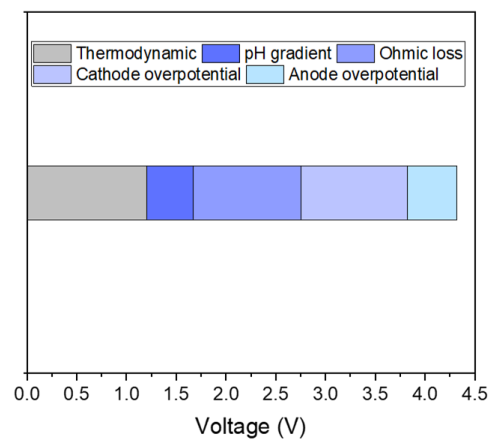
Fig. S19. Breakdown of the experimentally obtained applied voltage in acidic slim flow cell at 1.2 A/cm².

Table S6. Comparison of the carbon efficiency of our acidic media electrolyzer with those of benchmark alkaline and neutral CO$_2$R electrolyzers from literature.

Electrolyte pH, products	Single pass carbon efficiency (%)	Reference
pH ~ 7, CO	47.5	11
pH ~ 7, CO	33.1	12
pH ~ 14, CO	8.2	13
pH ~ 14, CO and C$_{2+}$	10.4	15
pH ~ 14, CO, formate and C$_{2+}$	22.5	14
pH ~ 15, C$_2$H$_4$	2.2	10
pH ~ 15, C$_2$H$_4$	4.5	7
pH ~ 1, CO, formate and C$_{2+}$	**77.4**	**This work**

References and Notes

1. S. Chu, A. Majumdar, Opportunities and challenges for a sustainable energy future. *Nature* **488**, 294–303 (2012). doi:10.1038/nature11475 Medline

2. P. De Luna, C. Hahn, D. Higgins, S. A. Jaffer, T. F. Jaramillo, E. H. Sargent, What would it take for renewably powered electrosynthesis to displace petrochemical processes? *Science* **364**, eaav3506 (2019). doi:10.1126/science.aav3506 Medline

3. S. Ren, D. Joulié, D. Salvatore, K. Torbensen, M. Wang, M. Robert, C. P. Berlinguette, Molecular electrocatalysts can mediate fast, selective CO_2 reduction in a flow cell. *Science* **365**, 367–369 (2019). doi:10.1126/science.aax4608 Medline

4. Y. Wu, Z. Jiang, X. Lu, Y. Liang, H. Wang, Domino electroreduction of CO_2 to methanol on a molecular catalyst. *Nature* **575**, 639–642 (2019). [doi:10.1038/s41586-019-1760-8](doi:10.1038/s41586-019-1760-8) Medline

5. B. A. Rosen, A. Salehi-Khojin, M. R. Thorson, W. Zhu, D. T. Whipple, P. J. A. Kenis, R. I. Masel, Ionic liquid–mediated selective conversion of CO_2 to CO at low overpotentials. *Science* **334**, 643–644 (2011). doi:10.1126/science.1209786 Medline

6. H. Xu, D. Rebollar, H. He, L. Chong, Y. Liu, C. Liu, C.-J. Sun, T. Li, J. V. Muntean, R. E. Winans, D.-J. Liu, T. Xu, Highly selective electrocatalytic CO_2 reduction to ethanol by metallic clusters dynamically formed from atomically dispersed copper. *Nat. Energy* **5**, 623–632 (2020). [doi:10.1038/s41560-020-0666-x](doi:10.1038/s41560-020-0666-x)

7. F. P. García de Arquer, C.-T. Dinh, A. Ozden, J. Wicks, C. McCallum, A. R. Kirmani, D.-H. Nam, C. Gabardo, A. Seifitokaldani, X. Wang, Y. C. Li, F. Li, J. Edwards, L. J. Richter, S. J. Thorpe, D. Sinton, E. H. Sargent, CO_2 electrolysis to multicarbon products at activities greater than 1 A cm^{-2}. *Science* **367**, 661–666 (2020). doi:10.1126/science.aay4217 Medline

8. W. Ma, S. Xie, T. Liu, Q. Fan, J. Ye, F. Sun, Z. Jiang, Q. Zhang, J. Cheng, Y. Wang, Electrocatalytic reduction of CO_2 to ethylene and ethanol through hydrogen-assisted C–C coupling over fluorine-modified copper. *Nat. Catal.* **3**, 478–487 (2020). [doi:10.1038/s41929-020-0450-0](doi:10.1038/s41929-020-0450-0)

9. J. A. Rabinowitz, M. W. Kanan, The future of low-temperature carbon dioxide electrolysis depends on solving one basic problem. *Nat. Commun.* **11**, 5231 (2020). [doi:10.1038/s41467-020-19135-8](doi:10.1038/s41467-020-19135-8) Medline

10. C.-T. Dinh, T. Burdyny, M. G. Kibria, A. Seifitokaldani, C. M. Gabardo, F. P. García de Arquer, A. Kiani, J. P. Edwards, P. De Luna, O. S. Bushuyev, C. Zou, R. Quintero-Bermudez, Y. Pang, D. Sinton, E. H. Sargent, CO_2 electroreduction to ethylene via hydroxide-mediated copper catalysis at an abrupt interface. *Science* **360**, 783–787 (2018). doi:10.1126/science.aas9100 Medline

11. T. Haas, R. Krause, R. Weber, M. Demler, G. Schmid, Technical photosynthesis involving CO_2 electrolysis and fermentation. *Nat. Catal.* **1**, 32–39 (2018). [doi:10.1038/s41929-017-0005-1](doi:10.1038/s41929-017-0005-1)

12. R. B. Kutz, Q. Chen, H. Yang, S. D. Sajjad, Z. Liu, I. R. Masel, Sustainion imidazolium-functionalized polymers for carbon dioxide electrolysis. *Energy Technol.* **5**, 929–936 (2017). doi:10.1002/ente.201600636

13. S. Verma, Y. Hamasaki, C. Kim, W. Huang, S. Lu, H.-R. M. Jhong, A. A. Gewirth, T. Fujigaya, N. Nakashima, P. J. A. Kenis, Insights into the low overpotential electroreduction of CO_2 to CO on a supported gold catalyst in an alkaline flow electrolyzer. *ACS Energy Lett.* **3**, 193–198 (2018). doi:10.1021/acsenergylett.7b01096

14. T. T. H. Hoang, S. Verma, S. Ma, T. T. Fister, J. Timoshenko, A. I. Frenkel, P. J. A. Kenis, A. A. Gewirth, Nanoporous copper–silver alloys by additive-controlled electrodeposition for the selective electroreduction of CO_2 to ethylene and ethanol. *J. Am. Chem. Soc.* **140**, 5791–5797 (2018). doi:10.1021/jacs.8b01868 Medline

15. S. Ma, M. Sadakiyo, R. Luo, M. Heima, M. Yamauchi, P. J. A. Kenis, One-step electrosynthesis of ethylene and ethanol from CO_2 in an alkaline electrolyzer. *J. Power Sources* **301**, 219–228 (2016). doi:10.1016/j.jpowsour.2015.09.124

16. D. W. Keith, G. Holmes, D. St. Angelo, K. Heidel, A process for capturing CO_2 from the atmosphere. *Joule* **2**, 1573–1594 (2018). doi:10.1016/j.joule.2018.05.006

17. M. Ma, E. L. Clark, K. T. Therkildsen, S. Dalsgaard, I. Chorkendorff, B. Seger, Insights into the carbon balance for CO_2 electroreduction on Cu using gas diffusion electrode reactor designs. *Energy Environ. Sci.* **13**, 977–985 (2020). doi:10.1039/D0EE00047G

18. F. Li, A. Thevenon, A. Rosas-Hernández, Z. Wang, Y. Li, C. M. Gabardo, A. Ozden, C. T. Dinh, J. Li, Y. Wang, J. P. Edwards, Y. Xu, C. McCallum, L. Tao, Z.-Q. Liang, M. Luo, X. Wang, H. Li, C. P. O'Brien, C.-S. Tan, D.-H. Nam, R. Quintero-Bermudez, T.-T. Zhuang, Y. C. Li, Z. Han, R. D. Britt, D. Sinton, T. Agapie, J. C. Peters, E. H. Sargent, Molecular tuning of CO_2-to-ethylene conversion. *Nature* **577**, 509–513 (2020). doi:10.1038/s41586-019-1782-2 Medline

19. C. J. Bondue, M. Graf, A. Goyal, M. T. M. Koper, Suppression of hydrogen evolution in acidic electrolytes by electrochemical CO_2 reduction. *J. Am. Chem. Soc.* **143**, 279–285 (2021). doi:10.1021/jacs.0c10397 Medline

20. Z. Wang, P. Hou, Y. Wang, X. Xiang, P. Kang, Acidic electrochemical reduction of CO_2 using nickel nitride on multiwalled carbon nanotube as selective catalyst. *ACS Sustain. Chem. Eng.* **7**, 6106–6112 (2019). doi:10.1021/acssuschemeng.8b06278

21. R. Kortlever, C. Balemans, Y. Kwon, M. T. M. Koper, Electrochemical CO_2 reduction to formic acid on a Pd-based formic acid oxidation catalyst. *Catal. Today* **244**, 58–62 (2015). doi:10.1016/j.cattod.2014.08.001

22. H. Ooka, M. C. Figueiredo, M. T. M. Koper, Competition between hydrogen evolution and carbon dioxide reduction on copper electrodes in mildly acidic media. *Langmuir* **33**, 9307–9313 (2017). doi:10.1021/acs.langmuir.7b00696 Medline

23. Y. Liu, C. C. L. McCrory, Modulating the mechanism of electrocatalytic CO_2 reduction by cobalt phthalocyanine through polymer coordination and encapsulation. *Nat. Commun.* **10**, 1683 (2019). doi:10.1038/s41467-019-09626-8 Medline

24. Y. Wu, K. Kamiya, T. Hashimoto, R. Sugimoto, T. Harada, K. Fujii, S. Nakanishi, Electrochemical CO_2 reduction using gas diffusion electrode loading Ni-doped covalent triazine frameworks in acidic electrolytes. *Electrochemistry* **88**, 359–364 (2020). doi:10.5796/electrochemistry.20-64036

25. J. Shen, R. Kortlever, R. Kas, Y. Y. Birdja, O. Diaz-Morales, Y. Kwon, I. Ledezma-Yanez, K. J. P. Schouten, G. Mul, M. T. M. Koper, Electrocatalytic reduction of carbon dioxide to carbon monoxide and methane at an immobilized cobalt protoporphyrin. *Nat. Commun.* **6**, 8177 (2015). doi:10.1038/ncomms9177 Medline

26. I. Katsounaros, J. C. Meier, S. O. Klemm, A. A. Topalov, P. U. Biedermann, M. Auinger, K. J. J. Mayrhofer, The effective surface pH during reactions at the solid–liquid interface. *Electrochem. Commun.* **13**, 634–637 (2011). doi:10.1016/j.elecom.2011.03.032

27. N. Gupta, M. Gattrell, B. MacDougall, Calculation for the cathode surface concentrations in the electrochemical reduction of CO_2 in $KHCO_3$ solutions. *J. Appl. Electrochem.* **36**, 161–172 (2006). [doi:10.1007/s10800-005-9058-y](doi:10.1007/s10800-005-9058-y)

28. M. Jouny, W. W. Luc, F. Jiao, General techno-economic analysis of CO_2 electrolysis systems. *Ind. Eng. Chem. Res.* **57**, 2165–2177 (2018). doi:10.1021/acs.iecr.7b03514

29. A. Murata, Y. Hori, Product selectivity affected by cationic species in electrochemical reduction of CO_2 and CO at a Cu electrode. *Bull. Chem. Soc. Jpn.* **64**, 123–127 (1991). doi:10.1246/bcsj.64.123

30. S. Ringe, E. L. Clark, J. Resasco, A. Walton, B. Seger, A. T. Bell, K. Chan, Understanding cation effects in electrochemical CO_2 reduction. *Energy Environ. Sci.* **12**, 3001–3014 (2019). [doi:10.1039/C9EE01341E](doi:10.1039/C9EE01341E)

31. J. Resasco, L. D. Chen, E. Clark, C. Tsai, C. Hahn, T. F. Jaramillo, K. Chan, A. T. Bell, Promoter effects of alkali metal cations on the electrochemical reduction of carbon dioxide. *J. Am. Chem. Soc.* **139**, 11277–11287 (2017). doi:10.1021/jacs.7b06765 Medline

32. S. Ringe, C. G. Morales-Guio, L. D. Chen, M. Fields, T. F. Jaramillo, C. Hahn, K. Chan, Double layer charging driven carbon dioxide adsorption limits the rate of electrochemical carbon dioxide reduction on Gold. *Nat. Commun.* **11**, 33 (2020). [doi:10.1038/s41467-019-13777-z](doi:10.1038/s41467-019-13777-z) Medline

33. H. Zimmermann, R. Walzl, "Ethylene" in *Ullmann's Encyclopedia of Industrial Chemistry* (Wiley-VCH, 2009).

34. J. H. Montoya, C. Shi, K. Chan, J. K. Nørskov, Theoretical insights into a CO dimerization mechanism in CO_2 electroreduction. *J. Phys. Chem. Lett.* **6**, 2032–2037 (2015). doi:10.1021/acs.jpclett.5b00722 Medline

35. R. B. Sandberg, J. H. Montoya, K. Chan, J. K. Nørskov, CO-CO coupling on Cu facets: Coverage, strain and field effects. *Surf. Sci.* **654**, 56–62 (2016). doi:10.1016/j.susc.2016.08.006

36. A. Ozden, F. Li, F. P. García de Arquer, A. Rosas-Hernández, A. Thevenon, Y. Wang, S.-F. Hung, X. Wang, B. Chen, J. Li, J. Wicks, M. Luo, Z. Wang, T. Agapie, J. C. Peters, E. H. Sargent, D. Sinton, High-rate and efficient ethylene electrosynthesis using a

catalyst/promoter/transport layer. *ACS Energy Lett.* **5**, 2811–2818 (2020). doi:10.1021/acsenergylett.0c01266

37. D. S. Ripatti, T. R. Veltman, M. W. Kanan, Carbon monoxide gas diffusion electrolysis that produces concentrated C_2 products with high single-pass conversion. *Joule* **3**, 240–256 (2019). doi:10.1016/j.joule.2018.10.007

38. A. Ozden, Y. Wang, F. Li, M. Luo, J. Sisler, A. Thevenon, A. Rosas-Hernández, T. Burdyny, Y. Lum, H. Yadegari, T. Agapie, J. C. Peters, E. H. Sargent, D. Sinton, Cascade CO_2 electroreduction enables efficient carbonate-free production of ethylene. *Joule* **5**, 706–719 (2021). doi:10.1016/j.joule.2021.01.007

39. S. Weisenberger, A. Schumpe, Estimation of gas solubilities in salt solutions at temperatures from 273 K to 363 K. *AIChE J.* **42**, 298–300 (1996). doi:10.1002/aic.690420130

40. C. M. Gabardo, C. P. O'Brien, J. P. Edwards, C. McCallum, Y. Xu, C.-T. Dinh, J. Li, E. H. Sargent, D. Sinton, Continuous carbon dioxide electroreduction to concentrated Multi-carbon products using a membrane electrode assembly. *Joule* **3**, 2777–2791 (2019). doi:10.1016/j.joule.2019.07.021

41. T. Burdyny, W. A. Smith, CO_2 reduction on gas-diffusion electrodes and why catalytic performance must be assessed at commercially-relevant conditions. *Energy Environ. Sci.* **12**, 1442–1453 (2019). doi:10.1039/C8EE03134G

42. P. K. Das, X. Li, Z.-S. Liu, Effective transport coefficients in PEM fuel cell catalyst and gas diffusion layers: Beyond Bruggeman approximation. *Appl. Energy* **87**, 2785–2796 (2010). doi:10.1016/j.apenergy.2009.05.006

43. D. M. Bernardi, M. W. Verbrugge, Mathematical model of a gas diffusion electrode bonded to a polymer electrolyte. *AIChE J.* **37**, 1151–1163 (1991). doi:10.1002/aic.690370805

44. B. Kumar, J. P. Brian, V. Atla, S. Kumari, K. A. Bertram, R. T. White, J. M. Spurgeon, New trends in the development of heterogeneous catalysts for electrochemical CO_2 reduction. *Catal. Today* **270**, 19–30 (2016). doi:10.1016/j.cattod.2016.02.006

45. Y. Chen, N. S. Lewis, C. Xiang, Modeling the performance of a flow-through gas diffusion electrode for electrochemical reduction of CO or CO_2. *J. Electrochem. Soc.* **167**, 114503 (2020). doi:10.1149/1945-7111/ab987a